Optical Transition Rates in a Cylindrical Quantum Wire with Parabolic and Inverse Parabolic Electric Confining Potentials in a Magnetic Field

Moletlanyi Tshipa (tshipam@ub.ac.bw)
University of Botswana https://orcid.org/0000-0001-6894-7637
Monkami Masale
University of Botswana

Research Article

Keywords: Optical transition rates,cylindrical quantum wire,electric confining potential

Posted Date: June 18th, 2021

DOI: https://doi.org/10.21203/rs.3.rs-573174/v1

Optical and Quantum Electronics manuscript No.
(will be inserted by the editor)

Optical transition rates in a cylindrical quantum wire with a parabolic and inverse parabolic electric confining potential in a magnetic field

Moletlanyi Tshipa · Monkami Masale

Received: date / Accepted: date

Abstract Electron transition rates due to interaction with circularly polarized light incident along the axis of a free-standing solid cylindrical nanowire are evaluated in the dipole approximation. The electric confinement potential of the nanowire is modeled as a superposition of two parts, in general, of different strengths; viz; parabolic and inverse parabolic in the radial distance. Additional confinement of the charge carriers is through the vector potential of the axial applied magnetic field. In systems with cylindrical symmetry, the electronic states are in part characterized by azimuthal quantum numbers: $m = 0, \pm 1, \pm 2..$, which in the absence of the axial applied magnetic field are doubly degenerate. In the dipole approximation and for circularly polarized light the selection rules are such that optical transitions are allowed between electronic states whose azimuthal quantum numbers differ by unity. Transition rates are characterized by peaks whenever the energy of the incident electromagnetic radiation matches transition energies for states between which transitions occur. The parabolic potential blue shifts peak of transition rates while the inverse parabolic potential redshifts the peaks. Results also indicate that transition rates are higher in nanowires of smaller radii. The homogeneous magnetic field lifts the double-degeneracies of electrons with opposite angular momenta, which leads to the emergence of two branches of the transition rates.

M. Tshipa
University of Botswana, Private Bag 0022, Gaborone, Botswana
Tel.: +267-3552140
Fax: +267-3185097
E-mail: tshipam@ub.ac.bw
ORCID: 0000-0001-6894-7637

M. Masale
University of Botswana, Private Bag 0022, Gaborone, Botswana
Tel.: +267-3554711
Fax: +267-3185097
E-mail: masalem@ub.ac.bw

Keywords Optical transition rates · cylindrical quantum wire · electric confining potential

1 Introduction

Confinement of the charge carriers is crucial in the design of nanodevices because of inherent quantum effects. Quantum confinement is possible due to nanofabrication techniques like molecular beam epitaxy (Li et al., 2016; Gómez et al., 2019), lithography (Williams et al., 2018), chemical vapour deposition (Hatta et al., 2017; D. et al., 2018), among others. These techniques enable fabrication of nanostructures of different geometries, for example, cylinders (Kim and No, 2017; Giammaria et al., 2018; Foster et al., 2019), spheres (Ahmed et al., 679; Malm and Vesikari, 2017), tetrapods (Rahman et al., 2017), and so forth. These nanostreuctures are central to the operation of nanodevices, and have applications in medicine (Batul et al., 2017), sensors (Wang et al., 2016; Leonardi, 2017), optoelectronics (Wada, 2000; Lin et al., 2019), photoelectrochemical (Shen et al., 2018) and display (Panfil et al., 2018) applications, among others.

In all these applications, the ability of electrons to transition from one state to the other plays a pivotal role. Clearer understanding of the rate at which these transitions occur is crucial in the design of nanodevices. In quantum computing, the speed of computations can be optimized from the understanding of the nature of transition rates (Funo et al., 2018). In biological or enzymatic process, understanding transitions rates between states is crucial in order to apply network design principles and in order to manipulate biological processes (Smith et al., 2016). There are a number factors that influence transition rates. Sasaki predicted increased speed of operation in nano-devices as a result of reducing their dimensionality (Sakaki, 1980), which has also been shown experimentally (Song et al., 2003). Electric confining potential intrinsic to nanostructures has been reported to modify both the magnitude of the rates as well as the energies at which peaks of transition rates occur (Tshipa and Masale, 2019). Externally applied electric or magnetic fields have also been shown to modulate transition rates through their corresponding confinement potentials (Li et al., 2018).

The aim of this work is to theoretically investigate the effect of externally applied magnetic field on optical transition rates in cylindrical quantum wires. The intrinsic electric confining potential of the quantum wire is considered to be a linear combination of the parabolic and inverse parabolic potentials. This type of a potential has been considered in the study of linear and non-linear optical properties of quantum discs (Duque et al., 2012; Niculescu et al., 2017; Liu et al., 2012). The inverse parabolic potential has also been studied in investigations of oscillator strength for optical transitions (Tshipa, 2014) and transition rates in the absence of externally applied magnetic field (Tshipa and Masale, 2019). According to our knowledge, effect of the linear combination of the parabolic and inverse parabolic potentials on transition rates

in the presence of an externally applied magnetic field has not been reported, which gives rise to drastically different properties of cylindrical quantum wires. This communication has the following organizational structure: Section 2 deals with the theory, Section 3 deals with the results and discussion thereof, while conclusions are laid in Section 4.

2 Theory

The system studied here is a very long solid cylinder of length L_z and radius R in a uniform magnetic field $\mathbf{B}$ applied parallel to the axis of the wire. The vector potential of the corresponding applied magnetic field is taken in the gauge $\mathbf{A} = (0, \frac{1}{2}B\rho, 0)$. The intrinsic confining potential of the quantum wire is taken in the form of a linear combination of the parabolic and inverse parabolic parts given by

$$V(\rho) = \begin{cases} \frac{1}{2}\mu\Big[\omega_{0p}^2\rho^2 + \omega_{0i}^2\Big(\frac{R^4}{\rho^2} - R^2\Big)\Big], & \rho < R \\ \infty, & \rho \geq R \end{cases} \tag{1}$$

where ω_{op} and ω_{oi} are the angular frequencies corresponding to the appropriate factors. These frequencies may be regarded as measures of strengths the corresponding forms of the potential. The Hamiltonian for the system considered here is cylindrically symmetric thence the wavefunction is taken in the general form: $\psi(\rho, \phi, z) = C_{ml}\chi(\rho)e^{ik_z z}e^{\iota m\phi}$, where $i = \sqrt{-1}$ is the unitary complex number, k_z is the axial wavenumber, C_{ml} the normalization constant of the corresponding azimuthal and radial quantum numbers m and l, respectively. The radial part of the electron's wave function satisfies the following differential equation:

$$\frac{1}{\rho}\frac{d}{d\rho}\Big(\rho\frac{d}{d\rho}\chi(\rho)\Big) + \Big\{\frac{2\mu}{\hbar^2}[E_{ml} - \frac{1}{2}m\hbar\omega_c - V(\rho)] - \frac{|m|^2}{\rho^2} - \frac{\mu^2\omega_c^2}{4\hbar^2}\rho^2\Big\}\chi(\rho) = 0, \tag{2}$$

where E_{ml} is the electron's subband energy and $\omega_c = eB/\mu$ is the electron's cyclotron frequency. The general solution of Eq. (2) is found in terms of a linear combination of the confluent hypergeometric functions M and U. The function U, however, has a divergent behavior at the origin $\rho = 0$ of the wire and is therefore discarded as a solution. To be more precise, the solution of equation that is well behaved for $0 \leq \rho \leq R$ is given by

$$\chi(\rho) = C_{ml}e^{-\xi/2}(\varsigma)^{|m|/2}M(a, b; \xi) \tag{3}$$

where

$$a = \frac{1 + \sqrt{m^2 + \mu^2\omega_{0i}^2R^4/\hbar^2}}{2} + \frac{E_{ml} - m\hbar\omega_c/2}{\hbar\sqrt{\omega_c^2 + 4\omega_{0p}^2}}, \tag{4}$$

$$b = 1 + \sqrt{m^2 + \mu^2\omega_{0i}^2R^4/\hbar^2} \tag{5}$$

and

$$\xi = \frac{\mu\sqrt{\omega_c^2 + 4\omega_{0p}^2}}{2\hbar}\rho^2. \tag{6}$$

Imposing the boundary condition of continuity of the wave function at $\rho = R$ gives the equation for the determination of the energy eigenvalues as

$$E_{ml} = \left(\frac{1 + \sqrt{m^2 + \mu^2\omega_{0i}^2 R^4/\hbar^2}}{2} - a_0\right)\hbar\sqrt{\omega_c^2 + 4\omega_{0p}^2} + \frac{1}{2}m\hbar\omega_c \tag{7}$$

where a_0 is the value of a which satisfies the explicit boundary condition of continuity of the wavefunction at $\rho = R$ given by $M(a_o, b; \xi_R) = 0$ with $\xi_R = \sqrt{\omega_c^2 + 4\omega_{0p}^2} \times (\mu R^2/2\hbar)$.

2.1 Transition rates

We consider circularly polarized electromagnetic radiation of energy ($\hbar\omega$) incident along the axis of the quantum wire. An electron can absorb an incident photon and transition from an initial state to a final state, provided that the energy of the photon is equal to the difference in energies of the initial and final states. The transition rate of the electron from an initial state ψ_i with energy E_i to a final state ψ_f with energy E_f is given by the Fermi Golden rule (Hashimzade et al., 2005)

$$W_{fi} = \frac{2\pi}{\hbar}|\langle\psi_f|H_{int}|\psi_i\rangle|^2\delta(E_f - E_i \pm \hbar\omega). \tag{8}$$

The electron-photon interaction H_{int} is given by

$$H_{int} = -\frac{e}{\mu}\vec{A_\omega}\cdot\vec{p} = -\frac{e}{2\mu}A_0[e^{i(\vec{q}\cdot\vec{r}-\omega t)} + e^{-i(\vec{q}\cdot\vec{r}-\omega t)}]\hat{\epsilon}\cdot\vec{p},$$

where $\vec{q}$ is the photon field wave vector, $\vec{r}$ the electron position vector, $\hat{\epsilon}$ is the unitary polarization vector of the radiation field and $A_0 = \sqrt{(N_q\hbar)/(2\epsilon_0\epsilon_m\omega V)}$ is the amplitude of the vector potential. N_q is the number of photons in volume V of the wire of dielectric constant ϵ_m and ϵ_0 is the permittivity of free space. Now, for circularly polarized light incident along the axis of the cylindrical wire, $\vec{q} = (0, 0, q_z)$ and $\hat{\varepsilon}\cdot\vec{r} = \rho(cos\phi \pm sin\phi)$, where the + (-) is for right (left) circular polarization. This gives the absorption and emission transition rates as

$$W_{fi}^{abs} = W_0|I_{m'l'ml}|^2\delta(E_f - E_i - \hbar\omega) \tag{9}$$

and

$$W_{fi}^{em} = W_0|I_{m'l'ml}|^2\delta(E_f - E_i + \hbar\omega), \tag{10}$$

respectively, where $W_0 = n_z e^2(E_f - E_i)^2/(\epsilon_0\epsilon_m\hbar^2\omega)$.

$$I_{m'l'ml} = \int_0^1 x^2 \chi^*_{m'l'}(x)\chi_{ml}(x)dx, \tag{11}$$

is the interaction integral and $x = \rho/R$. n_z is the photon linear density. For circularly polarized light and in the dipole approximation, the allowed transitions are only those for which the azimuthal quantum numbers of the initial and the final states differ by unity. These selection rules of optical transitions apply only to the azimuthal quantum numbers and with no restriction on the radial quantum numbers.

Now, for purposes of numerical calculations, the Dirac delta function has been replaced with a Lorentzian factor

$$\delta(E_f - E_i \pm \hbar\omega) \rightarrow \frac{\gamma}{\pi[(E_f - E_i \pm \hbar\omega)^2 + \gamma^2]},$$

in which γ is the so-called linewidth of resonance. The actual total transition rate of the quantum system involves a summation of all the individual transition rates, of course, taking into account the transition probabilities of all the allowed transitions. This is can be calculated from the following equations (Renk, 2012)

$$\Gamma^{abs}_{fi} = \sum W^{abs}_{fi} f_i(1 - f_f) \tag{12}$$

and

$$\Gamma^{em}_{fi} = \sum W^{em}_{fi} f_f(1 - f_i), \tag{13}$$

where f_i and f_f are the Fermi-Dirac distribution function, $f = \{1 + \exp[(E - E_F)/K_BT]\}^{-1}$, for the initial and final state respectively. Here, E_F is the Fermi energy of the crystal at temperature T and K_B is the Boltzmann's constant. The above equations can be used to evaluate rates of excitonic transitions, and with a number of factors taken into account. i) The band gap between the valence and the conduction band must be taken into account when evaluating the transition energies. ii) Appropriate wave functions should be used: those of the holes in the valence band and those of electrons in the conduction band under the Coulomb interaction, with proper effective masses for the electrons and holes (Singh and Oh, 2005). These values are of the order of picoseconds, for example, Citrin found $\approx 150\ ps$ for a cylindrical $GaAs$ quantum wire of radius 100 $\AA$ (Citrin, 1993).

3 Results and discussions.

This section is concerned with the discussions mainly of the influence of the different variations of the electric confinement potential and the applied magnetic field on the optical transition rates. It has to be said that the two parts of the intrinsic potentials tend to have opposite influences on the optical transition rates. For this reason, the influence of these parts of the intrinsic confinement

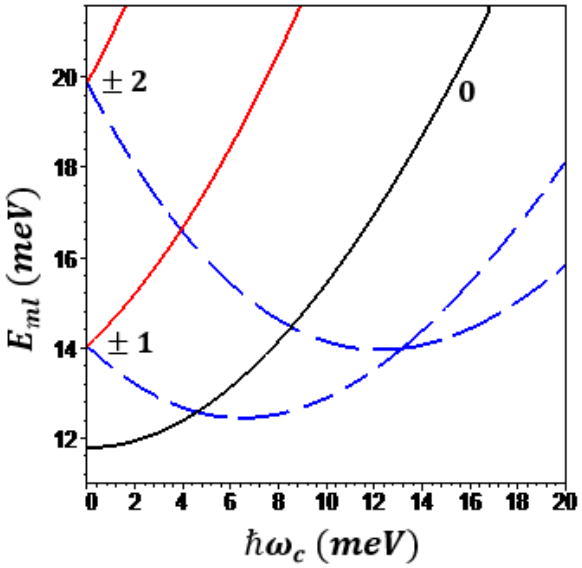

Fig. 1 The variations of some lowest-order $\ell = 1$ electron's energy subbands with the parallel applied magnetic field in a solid cylinder with an inverse parabolic electric potential. The key relevant parameters are: $R = 300\mathring{A}$, $\hbar\omega_{0p} = 0.0$ and $\hbar\omega_{0i} = 2.0\ meV$. The individual curves may be identified by the labels of the corresponding azimuthal quantum numbers: $m = 0, \pm 1$ and ± 2. The dashed plots are for the $m < 0$ states

potential on the transition rates is evaluated separately. The discussions, however, are limited to transitions only between the lowest electron's energy subbands; viz; $\{l = 1; m = 0\} \rightarrow \{l' = 1; m' = \pm 1\}$. Furthermore, only the results for the absorption process are shown for, brevity, since the functional forms of the absorption and the emission processes are very similar. The key parameters used for the computations here, and relevant to the system of $GaAs$ are $\mu = 0.67m_e$, $\epsilon_m = 12.5$, $E_F = 3\ meV$, $\gamma = 1\ meV$ and $n_z = 4.634 \times 10^9 m^{-1}$.

Figure 1 shows some of the lowest quantum number $\{\ell; \pm m\} = \{1, 0, \pm 1, \pm 2\}$ electron's energy subbands in a solid cylindrical quantum wire of radius $R = 300\mathring{A}$ with the parallel applied magnetic field. Here, the electric confinement potential of the quantum wire is taken as a special form of that given by equation (1), with the parabolic part 'switched off', that is, $\hbar\omega_{op} = 0$ but $\hbar\omega_{oi} = 2\ meV$. As is well known, in systems with cylindrical symmetry, the parallel applied magnetic field lifts the double degeneracy of the $m \neq 0$ energy subbands. The $m \geq 0$ electron's energy subbands increase with the increase of the magnetic field. The $m < 0$ energy subbands, however, initially decrease with the increase of the magnetic field and attain minima in their variations with the applied magnetic field. An additional feature of the electron's energy spectrum in a solid cylindrical quantum wire wherein the electric potential has an inverse parabolic variation with the radial distance. Such an electric potential tends to infinity near the axis of the quantum wire which results in a

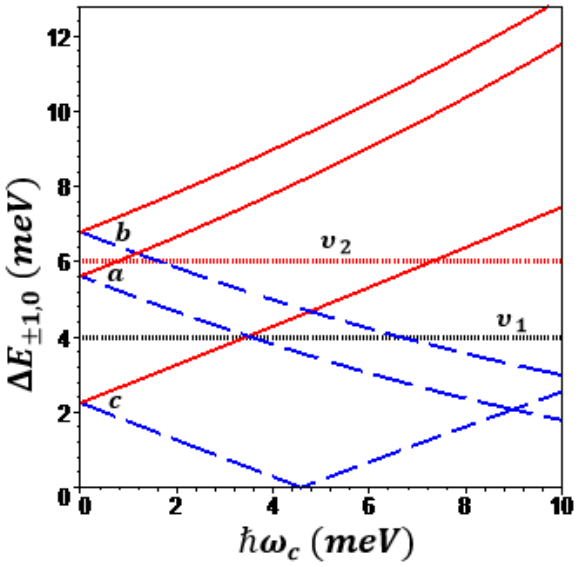

Fig. 2 The dependence of transition energies on the energy of the magnetic field in a quantum wire of radius $R = 300\mathring{A}$. The pair of plots marked a corresponds to an infinite cylindrical square well (ICQW) ($\hbar\omega_0 = 0$), b corresponds to a parabolic potential ($\hbar\omega_{0p} = 5\ meV$) superimposed on an ICQW while c is associated with an inverse parabolic potential ($\hbar\omega_{0i} = 2\ meV$) superposed on an ICQW

forbidden innermost region for the motion of electrons. Thus, for a wire with this type of potential, as the field increases, the $m < 0$ states take turns at becoming the ground state (that is, $m = -1, -2, -3, ...$). This is rather akin to the effect of the inner wall in cylindrical shell in a magnetic field (Masale et al., 1992) and electron-electron repulsion of confined electrons in a magnetic field (Wagner et al., 1951).

Figure 2 depicts the dependence of transition energies: $\Delta E = |E_f - E_i|$; on the magnetic field energy in a cylindrical quantum wire of radius $R = 300\mathring{A}$. The solid plots are transition energies between states $\{m = 0, l = l' = 1\}$ and $\{m' = 1, l = l' = 1\}$ while the dashed are for the $\{m = 0, l = l' = 1\} \rightarrow \{m' = -1, l = l' = 1\}$ transitions. The pairs of these curves with the same intercepts correspond to the different specific variations of the electric confining potential as follows: (a) Infinite Cylindrical Quantum Well (ICQW), corresponding to $\hbar\omega_{oi} = \hbar\omega_{op} = 0$; (b) parabolic potential solely ($\hbar\omega_{oi} = 0$) of strength such that $\hbar\omega_{op} = 5\ meV$ and (c) inverse parabolic potential only ($\hbar\omega_{op} = 0$) of strength $\hbar\omega_{oi} = 2\ meV$. Note that the inverse parabolic potential tends to dilate the electron's wavefunction and, in a sense, 'push' it towards the outer regions of the quantum wire. This is in contrast to the effect of the parabolic potential, which just like the vector potential of the magnetic field, tend to compress the electron's wavefunction towards the inner regions of the quantum wire. In the case of the inverse parabolic potential, the relative

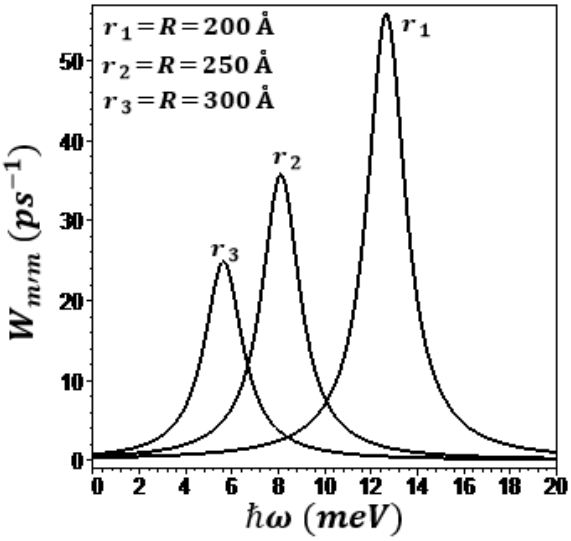

Fig. 3 The $m = 0 \rightarrow m = \pm 1$ optical transition rates as functions of incident radiation energy for cylindrical wires of radii $R = 150\mathring{A}$, $R = 200\mathring{A}$ and $R = 300\mathring{A}$. The other relevant parameters are $\hbar\omega_c = 0\ meV$, $\gamma = 2\ meV$ and $\hbar\omega_{oi} = \hbar\omega_{op} = 0$

increase of the electron's energy with the increase of the magnetic field of the $m = 0$ subband is thus more pronounced than that of the $m = \pm 1$ subband. The opposite is true in the case of the parabolic potential alone. As such, the parabolic potential enhances transitions energies while the inverse parabolic potential reduces the transition energies (Tshipa, 2014). Now, by inference from Fig. 1, the transition energies corresponding to the ground state and the first excited state $\Delta E = |E_{-m} - E_{-m-1}|$ initially close but then open up again as the parallel applied magnetic field is increased. The absolute values of these transition energies therefore pass through a minimum of zero in their variations with the applied magnetic field at the respective cross-over points whenever the $-(m+1)th$ energy subband now becomes the ground state.

Figure 3 depicts the zero-magnetic field lowest-order $\{m = 0 \rightarrow |m| = 1\}$ optical transition rates of a ICQW of three different radii: $r_1 = R = 200\mathring{A}$, $r_2 = R = 250\mathring{A}$ and $r_3 = R = 300\mathring{A}$, as indicated in the inset. Each curve, for a given radius, is characterized by a peak. As stated earlier, a peak of a transition rate occurs whenever the photon energy matches the transition energy. Here, γ determines the width of the curves for the optical transition rates. Note that maxima occur at lower photon energies in quantum wires of larger radii. It is also worth noting that stronger transitions occur in a quantum wire of smaller radius. This is a feature consistent with Sakaki's (Sakaki, 1980) prediction of increased speeds of operation in nano-devices as a result of reduced dimensions. Maxima of the transition rates is found to occur at higher values of the photon energy for smaller radii of the quantum wire.

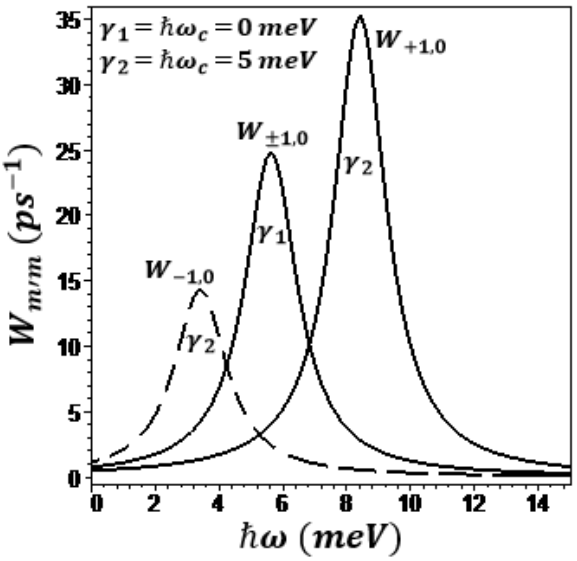

Fig. 4 Rates for the $m = 0 \rightarrow m = \pm 1$ optical transitions as functions of the energy of the radiation for an infinite cylindrical square well of radius $R = 300\mathring{A}$. The graph marked $W_{\pm 1,0}$ corresponds to $\hbar\omega_c = 0$, for either the $m = 0 \rightarrow m = 1$ or the $m = 0 \rightarrow m = -1$ transitions. The other curves correspond to $\hbar\omega_c = 5\ meV$

Figure 4 depicts the $\{m = 0 \rightarrow m = \pm 1\}$ transition rates as functions of photon energy for $\hbar\omega_c = 0\ meV$ (the middle curve) and for $\hbar\omega_c = 15\ meV$ for the other two curves. The additional relevant parameters are $R = 300\mathring{A}$ and $\hbar\omega_{oi} = \hbar\omega_{op} = 0$. It is seen that the variation of the transition rates with $\hbar\omega$ is similar to that shown in Fig. 3. In fact, the middle curve here is exactly the curve corresponding to $r_3 = R = 300\mathring{A}$ in Fig. 3, and is included here for reference. The key feature of this Fig. is that the application of the axial magnetic field splits the zero-field curve into the two branches flanking it. These branches of the transition rates emerge as a consequence of the lifting of the double-degeneracy of the $m \neq 0$ electron's energy subbands by the parallel applied magnetic field in a cylindrical quantum wire (Masale, 2000, 2008, 2002). Note also that the transition energies as well as the rates are higher for transitions involving $m = +1$ than those involving $m = -1$.

Figure 5 shows variations of the lowest-order $\{m = 0 \rightarrow |m| = 1\}$ optical transition rates with the photon energy in a quantum wire of radius $R = 300\mathring{A}$ in the absence of an applied magnetic field. The other relevant parameters are (a) $\hbar\omega_{oi} = \hbar\omega_{op} = 0$, (b) $\hbar\omega_{oi} = 0$; $\hbar\omega_{op} = 10\ meV$ and (c) $\hbar\omega_{oi} = 2\ meV$; $\hbar\omega_{op} = 0$. Since the parabolic potential increases transition energies, it blueshifts the peaks of transition rates. The inverse parabolic potential on the other hand deceases transition energies and hence redshift peaks of transition rates. Both potentials decrease the magnitude of the transition rates, with the inverse parabolic potential causing more decrease.

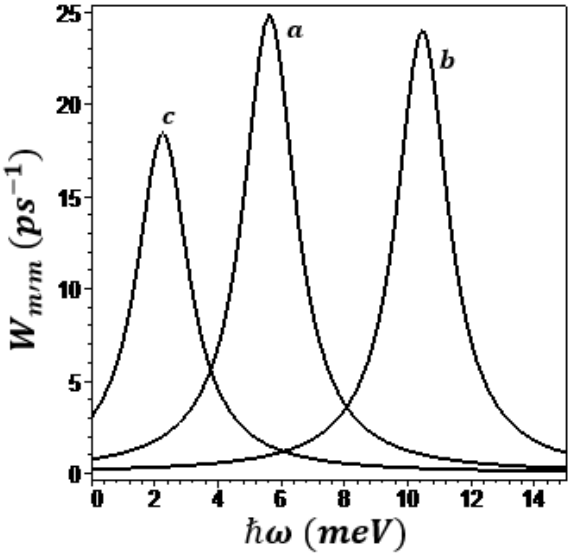

Fig. 5 The variation of $\{m = 0 \rightarrow m = \pm 1,\ l = l' = 1\}$ transition rates with the energy of the incident radiation field in the absence of the magnetic field. Radius of the quantum wire is $R = 300\mathring{A}$. The pair of plots marked a corresponds to an infinite cylindrical square well (ICQW) ($\hbar\omega_0 = 0$), b corresponds to a parabolic potential ($\hbar\omega_{0p} = 10\ meV$) superimposed on an ICQW while c is associated with an inverse parabolic potential ($\hbar\omega_{0i} = 2\ meV$) superposed on an ICQW

Fig. 6 shows the variations of optical transition rates with the photon energy in the absence of an applied magnetic field in a solid cylindrical wire of radius $R = 300\ \mathring{A}$. The additional parameters are the corresponding values of temperature used: $T = 100\ K$, $200\ K$ and $300\ K$, as indicated. The solid curves are transition rates evaluated by considering other subbands (according to Eq. 12) while the dash-dotted curve represents the $\{m = 0 \rightarrow m = \pm 1\}$ transition rates as calculated using Eq. 9. As temperature decreases, peaks of transition rates reduce in magnitude. This reduction is more apparent in peaks of transitions involving higher states. In fact, only up to the lowest 15 subbands have been considered when generating the summed rates in the figure, and inclusion of contributions of higher states yields no appreciable difference.

Figures 7 and 8 depict the dependence of $\{m = 0 \rightarrow m = \pm 1,\ l = l' = 1\}$ optical transition rates on the magnetic field energy for a quantum wire of radius $R = 300\mathring{A}$. In both figures, the solid plots are rates of $\{m = 0 \rightarrow m = 1,\ l = l' = 1\}$ transitions while the dashed plots are $\{m = 0 \rightarrow m = -1,\ l = l' = 1\}$ optical transition rates. The pairs of plots labelled 'a' correspond to an ICQW ($\hbar\omega_{0p} = \hbar\omega_{0i} = 0$), that labelled '$b$' corresponds to a parabolic potential ($\hbar\omega_{0p} = 5\ meV$, $\hbar\omega_{0i} = 0$) superimposed on an ICQW, while 'c' is associated with the inverse parabolic potential ($\hbar\omega_{0i} = 2\ meV$, $\hbar\omega_{0p} = 0$), superimposed on an ICQW. In Fig. 7, the energy of incident radiation is $\nu_1 = \hbar\omega = 4$

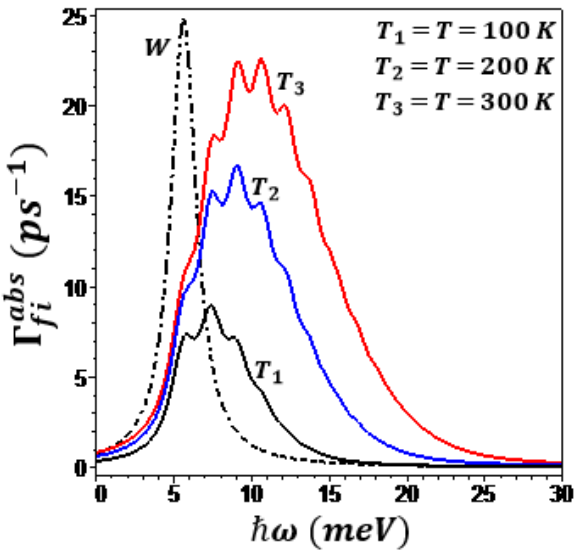

Fig. 6 The total scattering rates (solid plot) in a cylindrical quantum wire of radius $300\mathring{A}$ at temperatures $T_1 = T = 100\ K$, $T_2 = T = 200\ K$ and $T_3 = T = 300\ K$, as functions of energy of the incident EM radiation, as calculated according to Eq. 12. The dash-dotted are rates for transitions from the $m = 0$ state to the $m = \pm 1$ states, as calculated using Eq. 9. Here, $\hbar\omega_{0p} = \hbar\omega_{0i} = \hbar\omega_c = 0$

meV, which is less than zero-field transition energies while for Fig. 8 it is $\nu_2 = \hbar\omega = 6\ meV$, which is greater than the zero-field transition energies. In the case where the beam energy is less than zero-field transition energies, increase in the magnetic field will induce transitions involving only the $m = 0$ and $m = -1$ electron's states. The situation is the other way around when the photon energy is greater than the zero-field transition energies. In that case, an increase of the magnetic field induces transitions involving only the $m = 0$ and $m = +1$ electron's states. With reference to Fig. 2, even though ν_1 is less than zero-field transition energies of an ICQW, it is greater than the zero-field transition energies for an ICQW with a superimposed inverse parabolic potential. This implies that in this case, as the magnetic field energy increases, only $\{m = 0 \rightarrow m = 1,\ l = l' = 1\}$ transitions will be possible. ν_2, which is greater than the zero-field transition energies for an ICQW, is nevertheless less than the zero-field transition energies for an ICQW with a superimposed parabolic potential. As such, in this case, the magnetic field can induce only the $\{m = 0 \rightarrow m = -1,\ l = l' = 1\}$ transitions.

The values of transition rates obtained here are comparable to those obtained experimentally. For example, Bellesa *etal*. deduced excitonic lifetimes of 350 picoseconds (ps) from photoluminescence measurements in $GaAs/AlxGa_{1-x}As$ quantum boxes of length $L = 40\ nm$ formed on a V-grooved GaAs substrate, at a temperature of 6 K (Bellessa et al., 1998). Lifetimes are inverses of transition rates. Since the geometry is different from the one studied here, to compare the

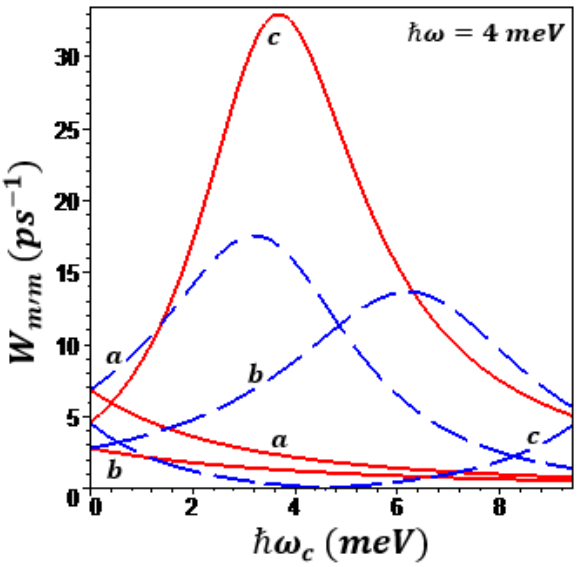

Fig. 7 Optical transition rates as functions of the magnetic field energy for a solid cylindrical nanowire of radius $R = 300\mathring{A}$ for photon energy of $\hbar\omega = 4\ meV$. The dashed curves represent rates for the $m = 0 \rightarrow m = -1$ transitions while the solid plots are for the $m = 0 \rightarrow m = 1$ transitions

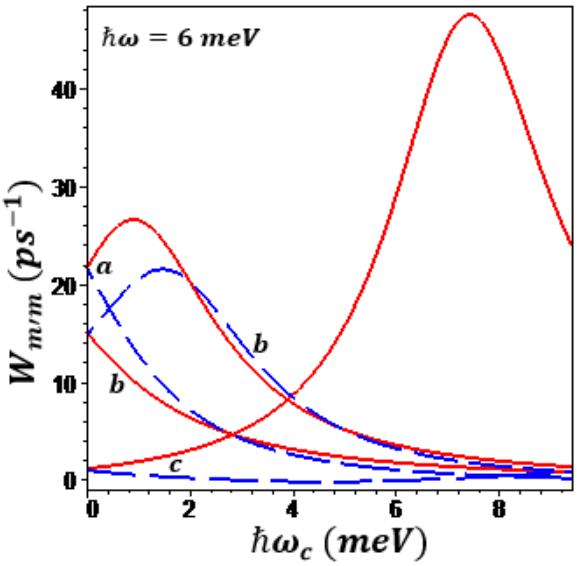

Fig. 8 Same as for figure 7 but with $\hbar\omega = 6\ meV$

two we consider the radius of a quantum wire that would have the same cross-sectional area as the QB considered by Bellesa *et al.*, that is $R = L/\sqrt{\pi} \approx 226$ $\mathring{A}$. With this value of the radius, using Eq. 12 in conjunction with the full width at half maximum of $\gamma = 8\ meV$, we obtained peaks of transition rates of $0.00264/ps$ corresponding to lifetimes of $379.3\ ps$. Akiyama *et al.* carried out photoluminescence measurements in $GaAs$ rectangular quantum wires grown by molecular beam epitaxy (Akiyama et al., 2005). In the paper, the authors investigate the effect of temperature on radiative lifetimes. Similar to comparison with the QB above, we consider a radius that will give same cross-sectional area as the one studied by Akiyama *et al.*, that is, $R = \sqrt{L_x L_y/\pi} \approx 72\ \mathring{A}$, where $L_x = 9\ nm$ and $L_y = 18\ nm$ are the dimensions of the quantum wire. Using a broadening of $\gamma = 10\ meV$ and a temperature of $T = 77\ K$, we obtained peaks of transition rates of $0.00169/ps$ (corresponding to lifetimes of $591\ ps$), compared with the value of $600\ ps$ obtained experimentally Akiyama *et al.* Melliti *et al.* obtained lifetimes in $InAs/GaAs$ quantum dots (Melliti et al., 2003) of around $800\ ps$. It is worth noting that the rates obtained in these experiments were for excitonic transitions.

4 Conclusions

Optical transition rates of a cylindrical quantum wire immersed in an axial applied magnetic field were evaluated within the effective mass and the dipole approximations. The radiation field was taken as that of circularly polarized light incident along the axis of the wire. The investigations here also included the influence of each of the two intrinsic confinement potential forms of the quantum wire on optical transition rates; parabolic or inverse parabolic in the radial distance. In systems with cylindrical symmetry, the angular momentum of an electron is quantized in integral multiples of m, the azimuthal quantum number. For circularly polarized light, and in the dipole approximation, the allowed optical transitions are only those for which the azimuthal quantum numbers of the initial and final states of the electron differ by unity. The investigations carried out here were limited to evaluation of the transition rates only between the lowest pairs of the azimuthal quantum numbers: $\{m = 0 \rightarrow m = \pm 1\}$. Overall, optical transitions rates were found to posses a characteristic peak in their variations with any of the relevant parameters. These resonance peaks occur whenever the photon energy matches exactly the electron's energy separations of the subbands involved in the optical transitions. The specific character of the electron's energy subbands, and therefore the energy separation between these, is determined by the overall confinement potential of the system considered. The parabolic potential has a tendency to blueshift peaks of optical transition rates, while the inverse parabolic potential redshifts peaks of optical transition rates. The axial applied magnetic field lifts the double degeneracy of the $m \neq 0$ electron's states, and consequently the emergence of the two optical transition rates corresponding to the $m = -1$ and $m = +1$ electron's final states. Results also indicate that transition rates

diminish as temperature decreases, and this reduction is more pronounced for transitions involving higher states. The results of these investigations suggest that the overall confinement of a nanosystem and temperature can be useful in the tuning of nanodevices in the regime of appropriate wavelengths.

Declarations

Funding: Not applicable.
Conflict of Interest: The authors declare that they have no conflict of interest.
Availability of data and material: Not applicable.
Code availability: Not applicable.

References

Ahmed, B., Kumar, S., Kumar, S., and Ojha, A. K. (679). Shape induced (spherical, sheets and rods) optical and magnetic properties of cds nanostructures with enhanced photocatalytic activity for photodegradation of methylene blue dye under ultra-violet irradiation. *J. Alloy. Compd.*, 2016:324–334.

Akiyama, H., Koshiba, S., Someya, T., Wada, K., Noge, H., Nakamura, Y., Inoshita, T., Shimizu, A., and Sakaki, H. (2005). Thermalization effect on radiative decay of excitons in quantum wires. *Phys. Rev. Lett.*, 72(6):924–927.

Batul, R., Tamanna, T., Khaliq, A., and Yu, A. (2017). Recent progress in the biomedical applications of polydopamine nanostructures. *Biomater. Sci.*, 5:1204.

Bellessa, J., Voliotis, V., Grousson, R., Wang, X. L., Ogura, M., and Matsuhata, H. (1998). Quantum-size effects on radiative lifetimes and relaxation of excitons in semiconductor nanostructures. *Phys. Rev. B*, 58(15):9933–9940.

Citrin, D. S. (1993). Excitonic spontaneous emission in semiconductor quantum wires. *IEEE ournal of Quantum Electronics, VOL. . NO. . JUNE*, 29(6):2117–2122.

D., J., Ironside, D. J., Bank, S. R., Gossard, A. C., and Bowers, J. E. (2018). Effect of growth interruption in 1.55 µm inas/inalgaas quantum dots on inp grown by molecular beam epitaxy. *J. Appl. Phys.*, 123:205302.

Duque, C. M., Mora-Ramos, M. E., and Duque, C. A. (2012). Quantum disc plus inverse square potential. an analytical model for two-dimensional quantum rings: Study of nonlinear optical properties. *Ann. Phys. (Berlin)*, 524(6–7):327–337.

Foster, J. C., Varlas, S., Couturaud, B., Coe, Z., and O'Reilly, R. (2019). Getting into shape: Reflections on a new generation of cylindrical nanostructures' self-assembly using polymer building blocks. *J. Am. Chem. Soc.*, 141:2742–2753.

Funo, K., Shiraishi, N., and Saito, K. (2018). Speed limit for open quantum systems. *New J. Phys.*, 21:013006.

Giammaria, J. T., Laus, M., and Perego, M. (2018). Technological strategies for self-assembly of ps-b-pdms in cylindrical sub-10 nm nanostructures for lithographic applications. *Advances in Physics: X*, 3:1445558.

Gómez, V. J., Santos, A. J., Blanco, E., Lacoix, B., Garcia, R., Huffaker, D. L., and Morales, F. M. (2019). Porosity control for plasma-assisted molecular beam epitaxy of gan nanowires. *Cryst. Growth Des.*, 19(4):2461–2469.

Hashimzade, F. M., Ismailov, T. G., and Mehdiyev, B. H. (2005). Influence of external transverse electric and magnetic fields on the absorption of a parabolic quantum wire. *Physica E*, 27:140–150.

Hatta, M. N. M., Hashim, M. S., Aida, S., Ainuddin, A. R., and Yunos, M. Z. (2017). Synthesis of carbon nanostructures from high density polyethylene (hdpe) and polyethylene terephthalate (pet) waste by chemical vapour deposition. *IOP Conf. Series: Journal of Physics: Conf. Series*, 914:012029.

Kim, .-H. and No, Y.-S. (2017). Subwavelength core/shell cylindrical nanostructures for novel plasmonic and metamaterial devices. *Nano Convergence*, 4:32.

Leonardi, S. G. (2017). Two-dimensional zinc oxide nanostructures for gas sensor applications. *Chemosensors*, 5:17.

Li, S. G., Gong, Q., Wang, X. Z., Cao, C. F., Zhou, Z. W. Shen, X. X., and He, K. (2016). Studies of inas/gaas quantum dot laser grown by gas source molecular beam epitaxy. *Opt. Quant. Electron.*, 48:131.

Li, X. J., Yu, J. H., Luo, K., Wu, Z. H., and Yang, W. (2018). Tuning the electrical and optical anisotropy of a monolayer black phosphorus magnetic superlattice. *Nanotechnology*, 29:174001.

Lin, C.-H., Cheng, B., Li, T.-Y., REtamal, J. R. D., Wei, T.-C., Fu, H.-C., Fand, X., and He, J.-H. (2019). Orthogonal lithography for halide perovskite optoelectronic nanodevices. *ACS Nano*, 13:1168–1176.

Liu, G., Guo, K., and Wang, C. (2012). Linear and nonlinear intersubband optical absorption in a disk-shaped quantum dot with a parabolic potential plus an inverse squared potential in a static magnetic field. *Physica B*, Volume 407(12):2334–2339.

Malm, M. and Vesikari, T. (2017). Rotavirus capsid vp6 tubular and spherical nanostructures act as local adjuvants when co-delivered with norovirus vlps. *Clin. Exp. Immunol.*, 189:331–341.

Masale, M. (2000). Oscillator strengths for optical transitions near a cylindrical cavity. *Physica B*, 291:256–265.

Masale, M. (2002). Electron states in quasi-one-dimensional structures; azimuthal applied magnetic field. *Phys. Scripta*, 65:459–464.

Masale, M. (2008). Electron-lo-phonon scattering near a current-carrying core. *Superlattice. Microst.*, 43:269–277.

Masale, M., Constantinou, N. C., and Tilley, D. R. (1992). Single-electron energy snbbands of a hollow cylinder in an axial magnetic field. *Phys. Rev. B*, 46(23):15432–15437.

Melliti, A., Maaref, M. A., Hassen, F., Hjiri, M., Maaref, H., Tignon, J., and Sermage, B. (2003). Radiative recombination lifetime of excitons in self-organized inas/gaas quantum dots. *Solid State Communications*, 128:213–217.

Niculescu, E. C., Stan, C., Tiriba, G., and Truşcă, C. (2017). Magnetic field control of absorption coefficient and group index in an impurity doped quantum disc. *Eur. Phys. J. B*, 90:100.

Panfil, Y. E., Oded, M., and Banin, U. (2018). Colloidal quantum nanostructures: Emerging materials for display applications. *Angew. Chem. Int. Ed.*, 57:4274 – 4295.

Rahman, R. A., arim, S. S. A., D., K., and Zulkifli, Z. (2017). Optical properties of tetrapod nanostructured zinc oxide by chemical vapour deposition. *J. Fundam. Appl. Sci.*, 9(5S):909–920.

Renk, K. F. (2012). *Basics of Laser Physics For Students of Science and Engineering*. Springer Science and Business Media.

Sakaki, H. (1980). Scattering suppression and high-mobility effect of size-quantized electrons in ultrafine. *Japanese Journal of Physics*, 19:L735.

Shen, S., Chen, J., Wang, M., Sheng, X., Chen, X., Feng, X., and Mao, S. S. (2018). Titanium dioxide nanostructures for photoelectrochemical applications. *Prog. Mater. Sci.*, 98:299–385.

Singh, J. and Oh, I.-K. (2005). Radiative lifetime of excitonic photoluminescence in amorphous semiconductors. *J. Appl. Phys.*, 97:063516.

Smith, R. W., Helwig, B., Westphal, A. H., Pel, E., H"orner, M., Beyer, H. M., Samodelov, S. L., Weber, W., Zurbriggen, M. D., Borst, J. W., and Fleck, C. (2016). Unearthing the transition rates between photoreceptor conformers. *BMC Syst. Biol.*, 10:110.

Song, H.and Wang, J., Chen, B., Peng, H., and Lu, S. (2003). Size-dependent electronic transition rates in cubic nanocrystalline europium doped yttria. *Chem. Phys. Lett.*, 376(1–2):1–5.

Tshipa, M. (2014). Oscillator strength for optical transitions in a cylindrical quantum wire with an inverse parabolic confining electric potential. *Indian J. Phys.*, 88:849–853.

Tshipa, M. and Masale, M. (2019). Optical transition rates in a cylindrical quantum wire with an inverse parabolic potential. *Adv. Theo. Comp. Phy.*, 2(2):1–5.

Wada, O. (2000.). Femtosecond semiconductor-based optoelectronic devices for optical-communication systems. *Opt. Quant. Electron.*, 32:453–471.

Wagner, M., Merkt, U., and Chaplik, A. V. (1951). Spin-singlet–spin-triplet oscillations in quantum dots. *Phys. Rev. B*, 45.

Wang, L., Sun, Y., Li, Z., Wu, A., and Wei, G. (2016). Bottom-up synthesis and sensor applications of biomimetic nanostructures. *Materials*, 9:53.

Williams, G., Hunt, M., Boehm, B., May, A., Taverne, M., Ho, D., Giblin, S., Read, D., Rarity, J., Allenspach, R., and Ladak, S. (2018). Two-photon lithography for 3d magnetic nanostructure fabrication. *Nano Res.*, 11(2):845–854.